# Liquid Water Transport and Management for Fuel Cells

Chapter 8

# Liquid water transport and management for fuel cells

**Anthony D. Santamaria[1], Prodip K. Das[2]**

[1]*General Motors, Global Propulsion Systems Pontiac Engineering Center, Pontiac, MI, USA,*

[2]*School of Engineering, The University of Edinburgh, Edinburgh, United Kingdom*

**Abstract**

Liquid water management is critical to proton exchange membrane fuel cell (PEMFC) performance and though the topic has received significant attention over the past couple of decades it remains a challenge as new materials and architectures are introduced in pursuit of higher efficiency and power densities. While water is necessary to facilitate efficient ionomer membrane function, its build-up in the liquid phase can saturate pores and reduce reactant gas diffusion rates. A primary challenge to liquid water transport at PEMFC length scales is that surface tension is dominant and so capillary effects at various interfaces must be understood and accounted for. Additionally, complex two-phase flow dynamics in the porous layers, as well as reactant channels, can have a large impact on overpotential and stability. This chapter discusses from a practical perspective liquid water production and transport in PEMFC systems, strategies to mitigate flooding, and new directions for the design and analysis of next-generation MEA and flow-field systems.

**Keywords:** Proton exchange membrane fuel cell (PEMFC); Water transport; Two-phase flow; Water management

## 1 Water production

Water in proton exchange membrane fuel cell (PEMFC) is produced in the cathode catalyst layer (cCL) as a result of the oxygen reduction reaction (ORR) with hydrogen and then transported through the diffusion media (gas diffusion layers (GDLs) and microporous layers (MPLs)) via two key mechanisms: convection and diffusion. Pressure differences drive convective fluid flow, while concentration gradients drive the diffusion process. For non-isothermal conditions, temperature-gradient-driven flow, also known as phase-change-induced (PCI) flow, also plays an important role in water transport in PEMFC (*1*, *2*). Understanding these processes in conjunction with the structure of each PEMFC layer, and the interfaces between them, is critical to developing an overall water balance picture.

The rate of water produced is directly proportional to the current density which can be expressed as:

$$\dot{m}_{H_2O} = \frac{i}{2F} M_{H_2O} \tag{8.1}$$

where $\dot{m}_{H_2O}$ is the mass flow rate of water, $i$ is current, $F$ is Faraday's constant, and $M_{H_2O}$ is the molecular weight of water. The cCL water content is dominated by the membrane and MPL uptake rates whose conditions can be controlled via cathode and anode reactant gas pressure, temperature, humidity, flow rate, and CL's wetting properties (*3*, *4*). When reactant gases become saturated, which is often the case under normal PEMFC operating conditions, condensation leads to liquid accumulation. The ratio of water contained in the gas phase can be determined by calculating the specific humidity, $\omega$:

$$\omega = \left(\frac{M_{H_2O}}{M_{Air}}\right) \frac{P_v}{P - P_v} \tag{8.2}$$

where $M_{Air}$ is the molecular weight of the non-water gas species (air for this example), $P$ is the total gas pressure, and $P_v$ is the saturation vapor pressure. The saturation pressure varies with temperature and can be obtained by looking them up in the reference tables in the ASHRAE Handbook. Condensation occurs when the partial pressure of water in the gas stream exceeds the saturation vapor pressure; the temperature at which this occurs is known as the dew point. Water, therefore, exists as a two-phase system, both a vapor and a liquid, throughout the membrane-electrode assembly (MEA) and gas flow channels (GC). The MEA in a fuel cell includes polymer

electrolyte (PE), CLs, MPLs, and GDLs. Two-phase flow can lead to liquid saturation of critical porous electrode regions which deleteriously affects oxygen diffusion rates and may lead to flooding as well as chemical and mechanical degradation. Conversely, proton conduction in the membrane depends on water; the electrolyte must remain well-hydrated to minimize ionic resistance. Overly dry conditions can lead to membrane dehydration which also negatively impacts PEMFC performance and lifetime. Therefore, developing strategies for PEMFC design and operation aimed at maintaining proper hydration while mitigating flooding has been, and continues to be, of prime importance. In this chapter, the processes associated with the transport of liquid water from CL to GC are discussed for each layer of the MEA and reactant channels which are outlined in Figure 8.1.

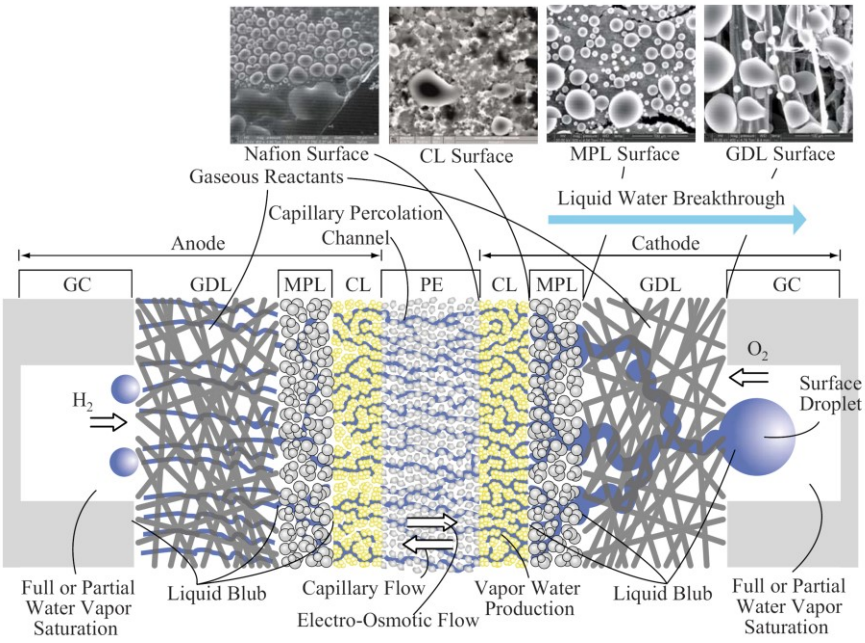


**FIGURE 8.1** Schematic diagram of water transport through PE (Nafion), CL, MPL, GDL, and GC porous layers highlighting capillary and electro-osmotic liquid water flows, water production by the electrochemical reaction, and percolation throughout all the layers. Environmental SEM images of water on PE, MPL, and GDL surfaces are also shown (*5*). *Credit: Reprinted from Hwang et al., Journal of The Electrochemical Society,* ***156****(10), B1192-B1200 (2009), with permission from the Electrochemical Society.*

## 2 Two-phase flow basics

Due to the small length scales of the MEA, capillary and viscous forces govern two-phase flow; the dimensionless parameters that quantify them are the capillary number, $Ca$, and viscosity ratio, $M$, defined as:

$$Ca = \frac{u\mu_{nw}}{\gamma} \tag{8.3}$$

and

$$M = \frac{\mu_{nw}}{\mu_{wet}} \tag{8.4}$$

respectively, where $u$ is the superficial velocity of the non-wetting phase, $\gamma$ is the surface tension, and $\mu_{wet}$ and $\mu_{nw}$ are the wetting and non-wetting phase viscosities. For PEMFC, liquid transport occurs predominately in the capillary fingering (CF) regime for hydrophobic pores (*6*). In the CF regime, the intruding fluid has a viscosity greater than the viscosity of the displaced fluid and the flow rate of the intruding fluid is low, as shown in the drainage phase diagram in Figure 8.2. Considering the in-plane percolation of the intruding fluid, the CF flow regime features the formation of a network of irregular conduits, or fingers, within the porous media. The presence of capillary-driven transport in these systems means that properties related to material wetting strongly influence transport behavior and can have large implications for electrochemical performance. Liquid imbibition in pores is governed by the Young-Laplace equation:

$$P_c = -\frac{2\gamma \cos\theta_s}{r} \tag{8.5}$$

where $P_c$ is the liquid capillary pressure, $\theta_s$ is the static liquid contact angle with the electrode surface, and $r$ is the liquid surface radius. Capillary-driven flow is always affected by pore structure and its hydrophobicity. Smaller radius droplets, for example, have a higher liquid pressure; therefore, they tend to be absorbed into larger droplets they encounter. Since GDL uptake of water results in liquid-filled pores unavailable to gas diffusion, it is useful to determine the relationship between capillary pressure and liquid saturation. Experimentally measured capillary pressure-water saturation curves (Figure 8.2b) show hysteresis between liquid uptake and withdrawal processes due to changing water pathways resulting from the dynamic nature of liquid interfaces (*7*, *8*). Another technique used to assess the barrier for liquid transport through a GDL is to measure breakthrough pressure (*9*, *10*). Breakthrough pressure is the maximum capillary pressure observed when injecting liquid through a GDL. During this process, pressure has been observed to build steadily until reaching a breakthrough point where pressure is relieved by droplet formation on the opposite surface (*11*, *12*). This method can capture the drainage process associated with fully saturated conditions where the liquid is the primary phase present in the GDL.

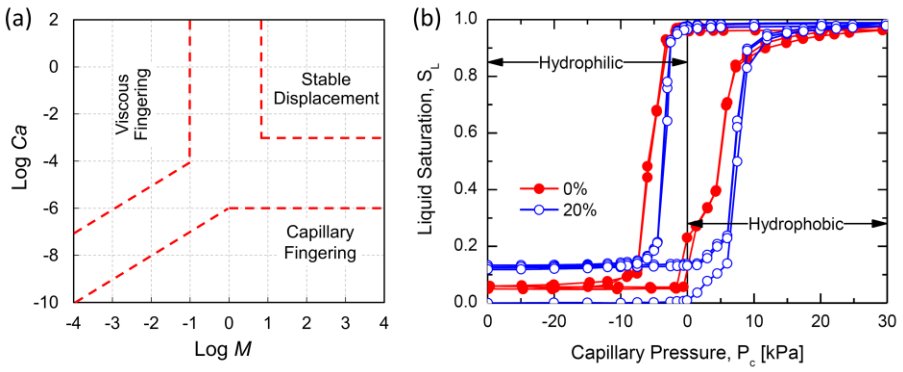


**FIGURE 8.2** (a) Drainage phase diagram showing key transport regimes. In PEMFC MEA, *Ca* between $10^{-8}$ to $10^{-5}$ and *M* around 17.5 is typical, indicating liquid water undergoes capillary-fingering within the porous media. (b) Example of typical liquid saturation vs. capillary pressure curves for two different PTFE loadings of GDL (*8*). *Credit: Reprinted from Das and Weber, Proc. of the ASME 11th Fuel Cell Science, Engineering and Technology Conference, Paper No. FuelCell2013-18010, pp. V001T01A002, (2013), with permission from the ASME.*

Liquid water that emerges from the GDL surface builds up in the flow channels as droplets. The liquid-gas two-phase flow patterns that occur in PEMFC channels typically fall under the categories of slug flow, and annular flow (*13*). Figure 8.3a shows closeups of these and other common flow patterns associated with PEMFC operation. Two-phase flow in PEMFCs is mainly dominated by the gas phase with mass flow quality, $x$, greater than 0.9. The mass flow quality, $x$, is defined as:

$$x = \frac{G_g}{G_l - G_g} \tag{8.6}$$

where $G_g$ and $G_l$ are gas-phase mass flux and liquid-phase mass flux, respectively (*14*, *15*). The mass flux is the product of phase density and superficial velocity. The two-phase flow regime observed in channels is directly linked to both air and liquid flow velocities. Figure 8.3b presents an overview of flow regime trends. Typically, higher gas velocities and lower liquid velocities trend toward single-phase conditions while lower gas velocities and higher liquid flow rates lead to droplets and slugs. Droplet formation is very common under a wide range of PEMFC operating conditions. Significant effort has been devoted toward understanding liquid droplet growth and removal from GDL surfaces as they can be a precursor to slug formation and channel flooding.

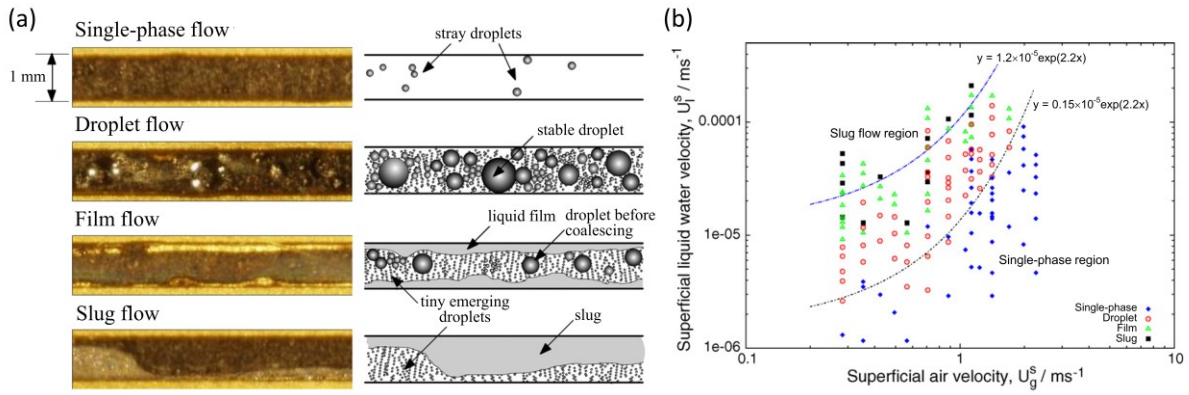


**FIGURE 8.3** (a) Overview of common two-phase flow patterns observed in PEMFC. (b) Two-phase flow regime trends relative to superficial gas and liquid velocities. *Credit: Reprinted from Hussaini et al., Journal of Power Sources, **187**(2), 444-451 (2009), with permission from Elsevier.*

Several models of droplet detachment have been proposed using a force balance between inertial, drag, and surface adhesion for simplified droplet geometries and aerodynamic drag correlations (*16*). Their development was motivated in part by the need to approximate the reactant channel gas speeds required for liquid removal. In general, droplet detachment vs. gas velocity curves have been shown to follow a power-law relationship; smaller droplets require significantly higher gas velocities for removal than larger ones. Adhesion force, sometimes referred to as the surface tension force, may be inferred by considering the line of contact between the droplet and GDL (assumed to be a circle where the sphere meets the GDL) and the dynamic angle, through the relationship:

$$F_{\gamma x} = \pi d\gamma \, sin^2 \, \theta_s \, sin \frac{1}{2}(\theta_a - \theta_r) \tag{8.7}$$

where $F_{\gamma x}$ is the surface tension force, $d$ is the wetted diameter, and $\theta_a$ and $\theta_r$ are the advancing and receding angles, respectively (*17*). Experimental validation usually relies on ex-situ transparent test channels where droplets are grown on the GDL and removed via flow gases while images of the droplet dynamics are captured for analysis. These models are useful for predicting droplet instability over a host of operational, design, and GDL surface treatment conditions (*18*). While the general agreement with experimental data is achieved, this adhesion approximation may be limiting as it relies on a single dynamic angle rather than a variable one and necessitates a complicated experimental setup. Numerical volume-of-fluid (VOF) models have also explored the incorporation of experimentally measured static and dynamic droplet angles which allowed for

reasonable estimation of droplet dynamics and detachment (*19*). The wetting of GDL surfaces is complex due to their inherent roughness and chemically heterogeneous surface which influence adhesion measurements. An alternative and simpler method for calculating liquid adhesion force to the GDL surface is to measure a droplet's sliding angle, which has been demonstrated by various techniques (*7*, *20*). Sliding angle, $\theta_s$, which refers to the angle at which a tilted droplet falls off due to gravity. The maximum adhesion, $f_a$, between the liquid and the surface can then be calculated as a ratio of gravity forces to approximated wetting perimeter:

$$f_a = \frac{\rho V g \sin\theta_s}{\pi d_w} \tag{8.8}$$

where $\rho$ is the liquid density, $V$ is the liquid volume, $g$ is gravity, and $d_w$ is the wetted diameter. Since adhesion is calculated on a force-per-length basis; the total adhesion force can be calculated by $F_\gamma = f_a \mu d_w$. This method can be employed by either directly pipetting droplets onto the GDL surface or by injecting water through the GDL to simulate in-situ liquid droplet formation. Figure 8.4a diagrams the technique and Fig. 8.4b shows the typical trend in sliding angle with respect to droplet volume for the two droplet formation methods. Usually, the GDL injection method requires a higher sliding angle for detachment corresponding to larger adhesion; further details are discussed in Refs. (*7*, *12*). Early work has shown the potential for using sliding-angle-based adhesion measurements to approximate droplet detachment as well as capture effects due to surface wetproofing, liquid flow rate variation, vibration, and aging (*12*, *21–23*).

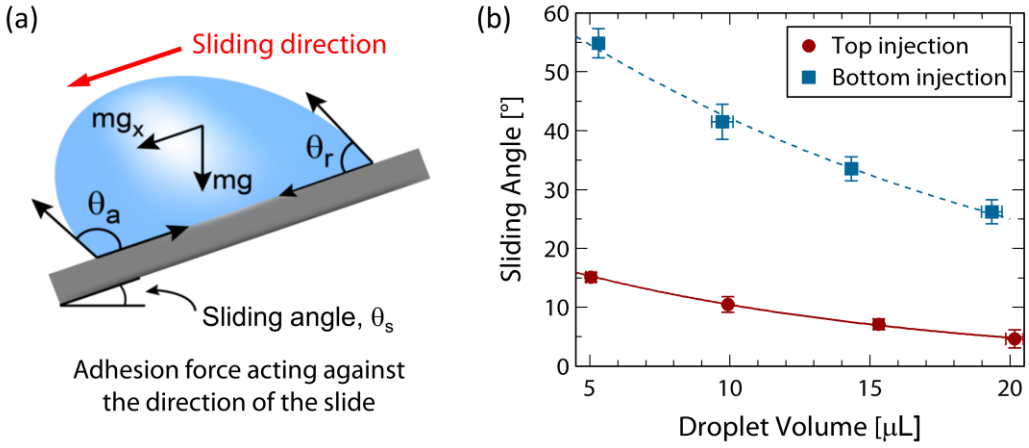


**FIGURE 8.4** (a) Schematic of a droplet undergoing the sliding angle test (b) Typical trends observed for sliding angle with respect to droplet volume as well as both pipetted (top injection) and through GDL injected droplets (bottom injection) (*7*). *Credit: Reprinted from Das et al., Journal of the Electrochemical Society,* ***159****(5), B489–B496, (2012), with permission from the Electrochemical Society.*

Several direct and indirect methods exist to investigate liquid-gas two-phase flow in fuel cell reactant channels. The former includes transparent cell analysis (*24*), X-ray tomography (*25*), Neutron imaging (including 2D radiography and 3D tomography) (*26*, *27*), and gas chromatography (*28*). While direct imaging offers far more certainty as to the distribution of liquid water, as depicted in Figure 8.5a, the limited beamline facilities, complicated setups, and high costs associated with these methods mean they are usually reserved for the highest priority studies. Indirect diagnostics, such as pressure drop, high-frequency resistance (HFR), and water mass accounting, offer simplified methods to study water's effects and may be combined with direct imaging (*29*). A major drawback to indirect methods is that they presently do not resolve the specific liquid distribution as well as imaging. One indirect method commonly employed relies on the two-phase flow pressure drop signal which is an immediate result of water accumulation in the flow channels. Studies may define a pressure amplification coefficient, $\varphi^2$:

$$\varphi^2 = \frac{\Delta P_{TP}}{\Delta P_{single-phase}} \tag{8.9}$$

which is the ratio of the actual measured two-phase pressure drop, $\Delta P_{TP}$, divided by the single-phase pressure drop, $\Delta P_{single-phase}$, for the gas phase (*30*). Overall, the two-phase pressure drop is considered a reliable in-situ diagnostic tool for monitoring the overall state of liquid water in PEMFC (*31*). A comprehensive review of two-phase pressure drop in PEMFC channels is available in Ref. (*32*). Despite significant efforts (*33–35*), an accurate prediction of two-phase flow pressure drop is still challenging. Theoretically, pressure drop ($\Delta P_{TP}$) for two-phase flow is a function of frictional ($\Delta P_F$), gravitational ($\Delta P_G$) and acceleration ($\Delta P_A$) pressure drops:

$$\Delta P_{TP} = \Delta P_F + \Delta P_G + \Delta P_A \tag{8.10}$$

The acceleration pressure loss is negligible due to the relatively low superficial gas velocities in PEMFC's flow channels. Gravitational pressure loss is also insignificant in channels due to the dominant influence of surface tension. Therefore, the frictional two-phase flow pressure drop is adequate to approximately explain the total pressure loss in PEMFC channels (*36*). Experimentally the two-phase pressure drop may be calculated, in-situ or ex-situ, by $\Delta P_{TP} = P_{in} - P_{out}$ which is the pressure difference between the inlet and outlet of a channel, flow field, or stack manifolds depending on testing scale. Figure 8.5b demonstrates time series ex-situ single channel two-phase

pressure trends at various water injection rates and at a fixed air flow rate. Reasonable predictions for the frictional two-phase flow pressure drop can be achieved through homogeneous equilibrium or separated flow models. The homogenous equilibrium model works well for high mass qualities, however, the model is not as useful for PEMFC applications (*35*). The separated flow model is based upon the summation of pressure gradients in the gas phase, liquid phase, and the interaction of gas-liquid, as shown in the equation below (*37*):

$$\left(-\frac{dp}{dz}\right)_{TP} = \left(-\frac{dp}{dz}\right)_f + \left(-\frac{dp}{dz}\right)_g + C\left[\left(-\frac{dp}{dz}\right)_f \left(-\frac{dp}{dz}\right)_g\right]^{1/2} \tag{8.11}$$

where $p$, $z$, and $C$ are the pressure, streamwise coordinate, and Chisholm parameter respectively. The subscripts $TP$, $f$, and $g$ represent two-phase, saturated liquid, and saturated vapor, respectively. The prediction accuracy depends significantly on Chisholm parameter, $C$ (*38*). This parameter is a function of multiple factors such as flow regime and capillary geometry (*39*). This empirical model has been shown to reasonably predict two-phase signatures for certain ranges of steady-state operation (*40*).

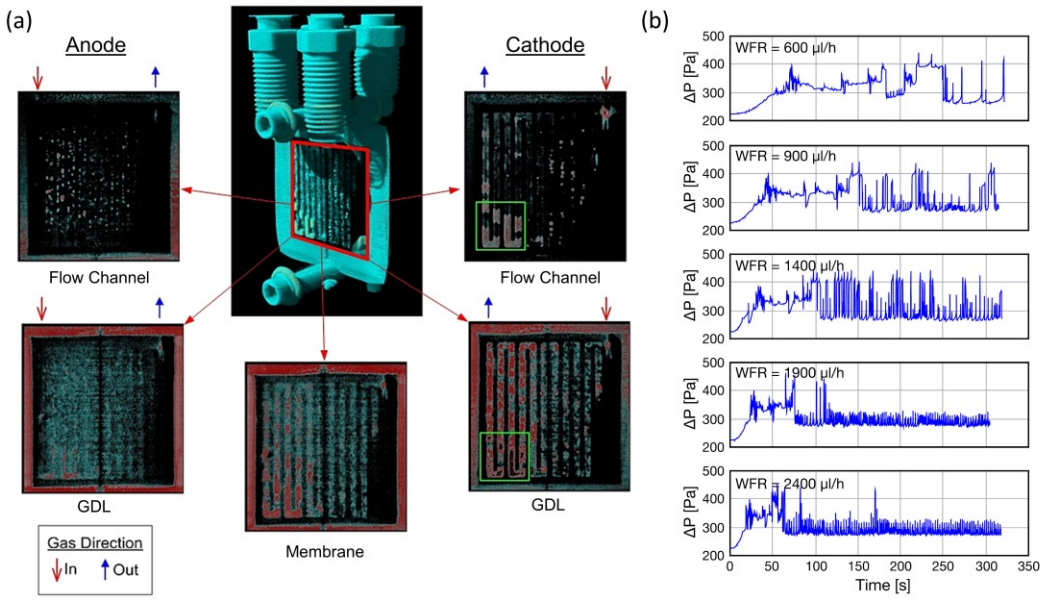


**FIGURE 8.5** (a) 3D Neutron tomography of a PEMFC (b) Ex-situ two-phase flow data for steady-state airflow and increasing water flow rate (WFR) through the GDL. *Credit: Reprinted from Tang et al., Journal of Power Sources, **195**(19), 6774-6781, (2010) and Niknam et al., Results in Engineering, **5**, 100071, (2020), with permission from Elsevier.*

Other numerical-based two-phase modeling efforts utilize VOF and Lattice-Boltzmann methods (LBM), among others, to simulate gas-liquid-solid interfaces and interactions. Studies have investigated liquid droplet formation and detachment predicted by VOF schemes and have demonstrated reasonable agreement with experimental data on the local level (*19*, *41*). Larger full-scale flow-field simulations are a challenge due to the increased computational domain size as well as complex boundary conditions, such as the rough GDL surface, which has a significant influence on liquid transport. The emergence of water from the GDL's randomly distributed fibrous and chemically heterogeneous surface leads to droplet pinning effects that are difficult to handle computationally and are of current interest to the research community (*42*). Two-phase modeling is necessary as single-phase models fail to capture the complex behavior resulting from liquid water physics in porous media and channels (*43*, *44*). The need for effective two-phase models is paramount to future PEMFC engineering where significant cost and time savings may be achieved during the design iteration process.

In assessing overall system performance for a PEMFC, the power consumption due to a two-phase pressure drop must be accounted for. The net system power (not accounting for humidification and other subsystems) can be calculated by subtracting the pumping power from the cell or stack power output (*45*). The pumping power is calculated using the inlet and outlet pressures of a PEMFC system. The following demonstrates the process applied to the cathode side. For the case of a standard air blower, the equations (*46*):

$$\dot{m}_{Air} = \frac{iA\xi_c}{4F}\left(\frac{M_{O_2}}{0.21}\right) \tag{8.12}$$

and

$$\dot{E} = \frac{\dot{m}_{Air} C_p T}{\eta}\left(\left(\frac{P_{in}}{P_{out}}\right)^{\frac{k-1}{k}} - 1\right) \tag{8.13}$$

maybe used to estimate power consumption, $\dot{E}$, where $A$ is the active cell area, $\xi_c$, is the cathode stoichiometry, $M_{O_2}$ is the molecular weight of oxygen, $C_p$ is the specific heat of air, $T$ is the blower inlet air temperature, $\eta$ is the pump efficiency, $P_{in}$ is the air pressure at the blower inlet (usually set to atmosphere), $P_{out}$ is the blower outlet pressure and $k$ is the specific heat ratio. The outlet pressure for the blower may be related to the inlet pressure of the fuel cell system which is directly

impacted by the two-phase pressure drop $\Delta P_{TP}$ of the cell. The parasitic effects of liquid buildup can be isolated by comparing the power required using the two-phase pressure signal to that of single-phase flow. For the total cell pumping power, the anode losses would also need to be considered in cases where a hydrogen pumping system is present.

## 3 PEMFC architecture

Traditional MEAs are multilayer architectures consisting of a polymer-electrolyte membrane (PEM), CLs, MPLs, and GDLs as highlighted in earlier chapters. For final assembly, each layer is laid up, and the MEA is formed via heat pressing. In a cell, gaskets are utilized to seal the MEA which is compressed between a set of flow fields or bipolar plates. The flow field contains the channels responsible for reactant delivery and product removal. Overall, the MPL and GDL are composed of randomly distributed carbon powder particles and fibers. Due to the current manufacturing process and hydrophobic treatment methods, MPLs and GDLs are chemically and structurally heterogeneous (*7*). Allowing effective gas diffusion while providing liquid pathways is a primary function for these layers. Studies have identified specific pore structures and distributions that could enhance liquid drainage and improve reactant delivery to catalyst sites; however, these designs are beyond standard manufacturing capabilities (*47*). The inability to control structure at these scales using current manufacturing methods and materials significantly limits technologies such as PEMFC from reaching full potential. MEA design and manufacturing remain large engineering challenges due to the small scales, complex interfaces, and specific material requirements. Nonlinearities due to highly coupled physical phenomena including thermal, fluid, and charge transport, highlight the need for MEAs to be studied in a holistic manner (*48*). The following sections discuss liquid transport on a layer-by-layer basis.

### 3.1 Membrane

Proton transport occurs through the ionic conducting polymer electrolyte membrane. While there are many variants, the commonly used persulfonated polytetrafluoroethylene (PTFE), a trade named Nafion, consists of a PTFE backbone with sulfonic acid ($SO_3^-H^+$) functional groups to facilitate charge transport. The ionic conductivity of Nafion is strongly dependent upon water content and increases with rising humidity. Therefore, maintaining a properly hydrated membrane is critical to electrochemical performance as well as preventing degradation. Liquid generated at

the cathode CL tends to back diffuse through the membrane toward the drier anode. This is opposed by the protons migrating from the anode to the cathode through a phenomenon known as electroosmotic drag as highlighted in the previous chapters. The balance of water within the membrane, as well as the net flux of water through it, is sensitive to and can be controlled by cathode and anode reactant conditions, electrode structure, and water generation rate (current density). Recently, a shift to thinner membranes has been pursued which promotes higher water back-diffusion from the cathode to the anode. Thinner membranes offer lower Ohmic losses while some drawbacks may be higher gas crossover rates and susceptibility to punctures.

### 3.2 Catalyst layer

The CL, which is sandwiched between the membrane surface and GDL, is a thin film of carbon-supported catalyst. Traditionally, CL material consists of several nanometer-sized particles of platinum deposited on carbon powder (such as Vulcan XC72) and then bound with an ionomer. The catalyst reduces the reaction activation energy while the carbon support and ionomer binder provide electron and proton conduction pathways, respectively. Product water forms in the cCL and, therefore, sufficient pore space must be available for liquid water to effectively permeate away from reaction regions to avoid gas blockages. The anode catalyst layer (aCL) also impacts cCL water migration by affecting back diffusion through the PEM. At higher temperatures, phase-change-induced water transport from the CL occurs in vapor form, however, at lower temperatures such as during startup, liquid formation may be unavoidable. A key goal of commercializing PEMFC technology is reducing platinum group metal (PGM) loadings while achieving increased power density. This can be partially accomplished by using thinner CLs. While typically a CL can be as thick as 30 μm current research into ultra-thin CL, targeting <1 μm, poses large challenges for water removal due to flooding sensitivity (*48*).

### 3.3 Microporous layer

The MPL serves a multifaceted role including providing a protective buffer between the GDL and membrane, enhancing electrical and thermal conductivity, and reducing interface liquid buildup. It is deposited directly onto the GDL surface and is usually composed of fine carbon powder as well as PTFE for hydrophobicity. This layer is typically less than 50 μm thick and has a porosity of ~50% with pore diameters ranging between 0.05 and 1 μm (*49*). Without an MPL, liquid tends to indiscriminately fill GDL pores at the CL interface which reduces oxygen and hydrogen

diffusion rates. The addition of an MPL has been shown to prevent such buildup by providing liquid-specific pathways, usually in the form of randomly distributed micro-cracks, that facilitate water transport while allowing smaller pores to remain open for gas diffusion.

Traditionally manufactured MPLs can be modified to improve performance. Methods usually entail providing effective pathways for gas and liquid transport. For example, small perforations in the MPL have been attributed to higher performance in PEMFC (*50*). The addition of larger micron-sized holes has been observed to favor liquid flow which prevents water from indiscriminately filling all pores at the MPL/GDL interface. Other recent work, diagramed in Figure 8.6a, has demonstrated the use of pore-forming agents which open randomly distributed micro-holes (~10 μm diameter) in the MPL (*51*). These modified MPLs were compared to an untreated MPL using fast operando X-ray tomographic microscopy (XTM) where it was confirmed the MPL with micro holes resulted in enhanced liquid drainage and oxygen transport. Such results agree with a growing consensus that larger holes better facilitate liquid flow while small pores enable gas diffusion. Similar improvements have also been achieved using perforated GDL (*52*). As these methods improve, controlling hole location and pattern may be of significance since MPL/GDL drainage may be affected by flow-field channel and rib locations.

### 3.4 Gas diffusion layer

The carbon paper, or sometimes carbon cloth, based GDL provides larger pores for liquid uptake from the CL or MPL and is usually coated with a hydrophobic treatment such as PTFE at 5-10% wt. loadings. Loadings higher than 10%, while available, have been shown to have minimal impact on hydrophobicity and may reduce performance as PTFE fills void space where liquid percolation or oxygen diffusion would occur (*12*). Typical pore sizes of GDL range from 10 to 100 μm. At these scales, capillary and viscous effects dominate two-phase flow. The CF flow regime associated with low liquid velocities observed in GDLs is characterized by the invasion of pores by the non-wetting fluid (in this case liquid water) by displacing the wetting fluid (reactant gases).

Under saturated vapor conditions, liquid builds up at the MPL/GDL interface. As the liquid pressure rises it forces the liquid front to fill pores following a path of least resistance; larger pores may be filled first as well as those with lower hydrophobicity. This results in a pattern of irregular conduits and branches propagating along with the GDL thickness that look like “fingers” for which this flow regime is named. As GDLs are 100 to 400 μm thick, liquid water may traverse dozens of

pores before reaching the GDL/channel interface. As the water begins to penetrate the GDL it encounters resistance due to capillary effects which cause the liquid pressure to increase. At some point, the pressure is enough to overcome the maximum resistance and a breakthrough occurs whereby water reaches the GDL/Channel interface (*12*). The maximum pressure, referred to as breakthrough pressure, is a commonly used measurement of a GDLs propensity for through-plane liquid transport. Lower breakthrough pressures may be desirable to facilitate liquid drainage. Thinner GDLs and reduced PTFE loadings have been shown to reduce breakthrough pressure (*12*). The amount and location of water for both in-plane and through-plane GDL directions are challenging to map due to the small feature sizes and opaque materials. Experimental methods utilizing neutron and x-ray imaging techniques have, more recently, uncovered capillary vs. saturation trends with such detail (*53*). Additionally, numerical pore network models, which apply interface physics to GDL structures to simulate water pathways, have been useful in identifying the impact of key GDL morphologies and properties on liquid saturation (*54–56*). GDL porosity is also affected by the flow-field compression which leads to reduced porosity beneath land or rib areas. Compression is necessary for good electrical contact between the plates and porous media; however, over-compression leads to GDL damage, higher pressure drop, and reduced performance (*57*). A compressed GDL will intrude into the channel which reduces the cross-sectional flow area while also reducing the angle between the GDL and channel wall leading to increased flow resistance for both gas and liquid phases. The interaction between the flow field and the GDL surface is also sensitive to temperature effects. For example, the location of coolant channels may cause temperature gradients which could cause liquid condensation in the local GDL.

In addition to adding perforations for liquid-specific pathways, as discussed in the MPL section, GDL designers have proposed pore gradient structured GDL to take advantage of the capillary-driven flow. Recently, groups have explored the use of transverse pore gradients for enhanced liquid drainage using electrospinning methods to create bi-layer GDL (*58*). As shown in Figure 8.6, the catalyst interfacing layer consisted of average pore diameter of about 175 nm while the channel interface layer's average pore diameter was about 687 nm. Using X-ray radiography, liquid water content was found to be reduced in the bi-layer GDL compared to a traditional GDL. Further discussion on advanced porous media is touched upon in Section 3.6.

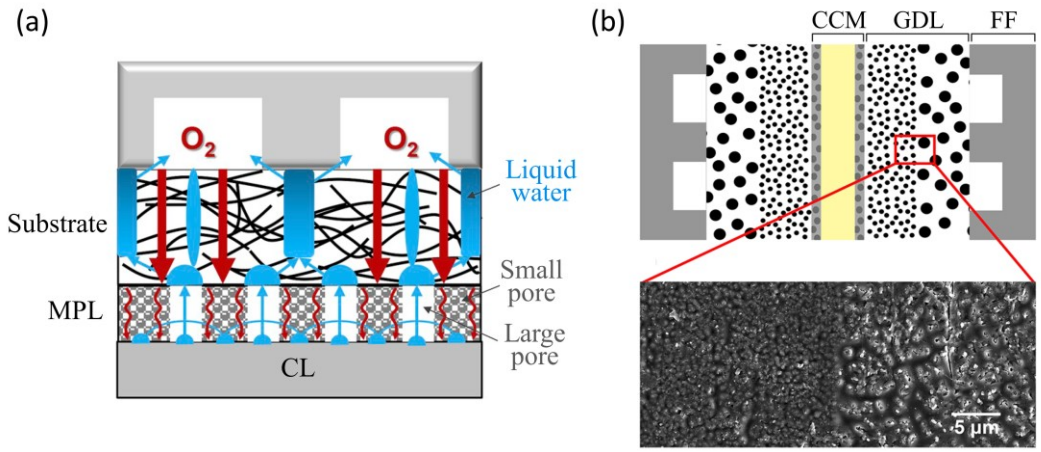


**FIGURE 8.6** (a) MPL holes for liquid drainage and (b) porous gradient in electro-spun bi-layer GDL. *Credit: Reprinted from Nagai et al., Journal of Power Sources, 435, 226809, (2019), with permission from Elsevier (part a) and Balakrishnan et al., ACS Appl. Energy Mater., 3, 2695–2707, (2020) (part b).*

## 4 Channels and flow fields

Channel geometry, including land width, channel width, and channel depth, significantly influences two-phase flow behavior and impacts PEMFC performance. Extensive in-situ experimental testing over a wide range of channel dimension combinations with depths and widths ranging from 0.25 mm to 1 mm has shown that optimal performance, accounting for pumping power at higher pressures, is achieved at a hydraulic diameter of ~0.4 mm for certain ranges of stoichiometry (*59*, *60*). Other results focusing on channel and rib widths (in parallel designs) have shown that narrower dimensions benefit high current density operation while wider benefit low current density conditions; overall, widths between 0.7 to 1 mm achieve a balance of high power and reduced manufacturing effort (*61*, *62*). 3D numerical simulation of interdigitated and parallel flow-field designs has demonstrated that sub 0.5 mm characteristic length channels were found to have the best performance which was attributed to improved water removal due to higher pressures (*63*). At ~0.5 mm peak performance is also achieved for square channel dimensions in interdigitated, serpentine, and spiral interdigitated designs (*64*). While they are increasingly powerful tools, and excellent at single-phase studies, larger-scale two-phase simulations should be supported by experimental verification when possible. Flow-field engineering usually requires extensive iteration between modeling, development, and testing to understand a new design's behavior. An overview of flow-field patterns, which play a significant role in liquid water build and the operating parameters, is presented in Figure 8.7. Traditional flow fields, which have been

studied extensively, include serpentine, parallel, and interdigitated. Over the past few decades, several other layouts have been proposed which are briefly introduced in the following.

***Serpentine flow field***: Serpentine flow patterns, consisting of either a long single path (Figure 8.7a) or multiple paths (Figure 8.7b), are effective at removing liquid water due to the higher pressure drop and gas velocities across the cell. However, a larger pressure drop across the cell can result in a significant concentration gradient between the inlet and outlet and high pumping losses. Pressure differences between adjacent channels induce crossflow through the GDL which can reduce diffusion lengths beneath land areas improving performance and reducing overall pressure drop (*65*). In these designs, the water content can be reduced at higher current densities, for stoichiometric-based flow, due to the elevated pressure drop forcing droplets from channels.

***Parallel flow field***: Parallel flow fields consist of a series of channels connected in parallel by an inlet and outlet manifold (Figure 8.7b). Generally, these have the lowest pressure drop due to a large effective cross-section for flow. Since the pressure drop across each channel is similar, convective crossflow between adjacent channels is minimal. This makes diffusion the dominant gas transport mechanism. In these designs, typically, narrower land widths and shallower channel depths are beneficial to performance (*39*, *66*). The lower pressure and multiple routes for reactant gases can lead to significant water accumulation and reactant maldistribution, especially under land areas where flooding can occur. Some of these issues may be overcome by using high aspect ratio designs (i.e., longer length channels) which results in higher gas velocities and pressure drop to force liquid removal. One benefit to parallel flow fields is that they can provide reduced pressure drop compared to more complicated designs (*43*, *44*, *67*). Thus, they are better suited for lower current density operation, and hybrid designs that shift between interdigitated (at high current density) have been demonstrated (*45*). Parallel flow fields may be improved by adding channel wave patterns which can enhance convective transport with minimal pressure drop (*68*).

***Interdigitated flow field***: While resembling parallel patterns, interdigitated inlet channels are not directly connected to the outlet channels (Figure 8.7d). This results in higher-pressure inlet channels driving reactant flow through the GDL to adjacent lower pressure outlet channels. While convective transport in the porous media has been shown to significantly boost electrochemical performance, these gains require higher pumping power. Interdigitated designs are especially sensitive to rib width, GDL properties, and compression. Studies have also shown a propensity for

inlet channel flooding in larger aspect ratio designs (*44*). Thus, further efforts are needed to improve the performance of interdigitated flow fields.

***Biomimetic/Fractal flow field***: Biological-inspired as well as fractal-based designs use patterns derived from nature to maximize gas delivery to the CL (Figure 8.7e). While a growing interest has motivated computational fluid dynamic modeling and theoretical studies focusing on optimization, understating these systems' performance is in the early stages (*69*, *70*). Given the complex geometry sometimes involved, a broader understanding of how these designs handle liquid water and perform in stacks is needed.

***Metal Foams and Meshes***: These offer alternatives to traditional channel and rib architectures (Figure 8.7f). Metal foam's high porosity, compressibility, and electrical conductivity make them potentially well-suited for PEMFC applications such as gas distributors and coolant channels (*71*, *72*). Metal foams have been demonstrated to provide even delivery of reactant gases and avoid the GDL liquid buildup associated with land areas (*73*). In several cases, foam-based flow fields have outperformed channel-based ones (*74*). One challenge related to liquid management is that a lack of channels to direct water may lead to water build-up in the foam pores. Recent work has focused on understanding liquid transport in foams as well as targeting solutions such as hydrophobic coatings to improve liquid drainage (*75*). Unlike foams, which have random pore structures, metal meshes can be manufactured with specific porous features. Toyota used 3D metal meshes for the cathode plates in the first-generation Mirai cells (*76*). Features such as baffling may be included to improve convective transport while providing pathways for liquid uptake from the GDL.

Single cells are combined to form stack assemblies, whereby, individual flow-field plates are connected via larger manifolds. These manifolds are responsible for bulk reactant delivery and exhaust and so must handle the net liquid water removed from all cells. Manifolds usually connect single cells in parallel; therefore, blockages in any single cell can lead to overall stack instability. For some systems, humid exhaust air is passed through a condenser to remove water which may be recycled for humidification. In vehicles such as the Toyota Mirai, excess liquid water is drained periodically (some models include a manual drain button).

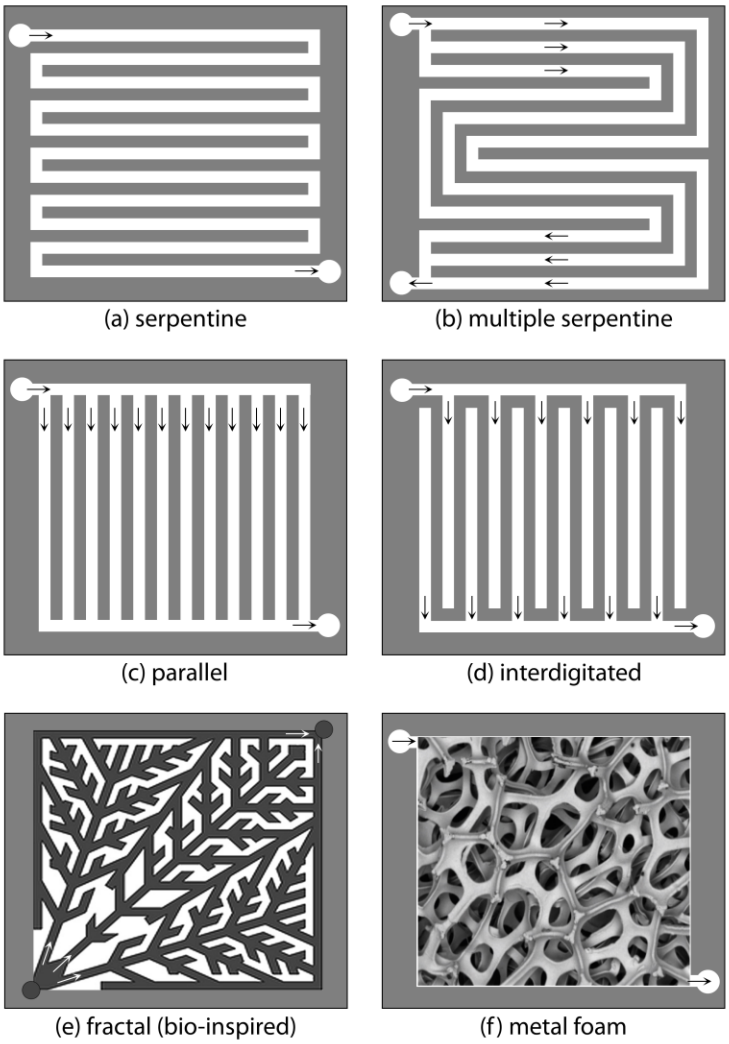


**FIGURE 8.7** Overview of different flow-field designs for PEMFCs. *Credit: Part (e) is adapted from Guo et al., International Journal of Hydrogen Energy, **39**(36), 21185-21195, (2014), with permission from Elsevier, and part (f) is adapted from Fly et al., Energies, **12**(7), 1186, (2019).*

The behavior of liquid water in PEMFC flow channels depends on the liquid-to-gas ratio, the superficial velocities of each phase, the surface characteristics of the channel and GDL, and the channel geometry. Pressure drop measured across the length of a channel is important as engineers seek to remove water with minimal parasitic energy consumption. Depending on the channel size, different forces can affect the transport mechanism of two-phase flow (*36*). Channels may be classified based on channel hydraulic diameter, $D_h$: (i) conventional channels $D_h > 3$ mm, (ii) minichannels 3 mm > $D_h$ > 200 μm, and (iii) microchannels 200 μm > $D_h$ > 10 μm (*77*). Modern PEMFC flow channels usually lie in the minichannel range while some channel features may be

on the microchannel scale. Liquid transport in PEMFC flow channels is capillary dominated as the dimensionless parameter Bond number is less than 1 (*13*). The Bond number, which is a ratio of gravitational acceleration effects to surface tension effects on the liquid-vapor interface, is defined as:

$$Bo = \frac{\rho g l^2}{\sigma} \tag{8.14}$$

where $\rho$ is the liquid density, $g$ is gravity, $l$ is the characteristic length and $\sigma$ is the surface tension. Due to the small characteristic length scale associated with the flow-field channels, the gravitational impact on the liquid-gas two-phase flow is insignificant (it may, however, have an impact in larger manifold regions). Another important parameter is the dimensionless Weber number:

$$We = \frac{\rho v^2 l}{\sigma} \tag{8.15}$$

where $v$ is the gas velocity. $We$ is the ratio of aerodynamic drag to capillary force. Liquid removal relies on aerodynamic drag; viscous and pressure forces must exceed liquid adhesion to channel and GDL surfaces for removal. Increasing gas velocity, associated with a higher Weber number, is a very effective method for managing liquid build-up, however, it leads to higher pressure and, therefore, higher parasitic power consumption by the blower or compressor.

Cross-sectional channel geometry impacts liquid uptake from the GDL surface to flow channels. Capillary wetting of channel/GDL corner regions is predicted by the Concus-Finn condition which depends on the hydrophobicity of the channel walls and GDL surface, as well as the draft angle between them (*78*). Rath et al. defined this limit for PEMFC applications as (*79*):

$$\theta_{wall} = (2\alpha + \pi) - \theta_{GDL} \tag{8.16}$$

where $\theta_{wall}$ is the limiting wall contact angle, $\theta_{GDL}$ is the GDL contact angle and $2\alpha$ is the open angle between the channel wall and GDL surface. This relationship can be used to determine the propensity for a channel design to wick water from GDL surfaces for improved water management (*80*). Results have shown that for typical GDL and hydrophilic flow channels, corner filling will not occur when $\alpha$ is 52° or smaller.

## 5 Liquid management concerns and strategies

To prevent porous media and channel flooding, liquid buildup must be continuously monitored and controlled. As discussed in prior sections, flooding can lead to reactant gas redistribution which causes performance instability and degradation. During operation, water accumulation may be monitored indirectly by sensors and controlled by adjusting gas flow rates, back pressure, cell temperature, gas humidity, and or current density. Additionally, there are many MEA and flow-field design strategies that have been explored to better accommodate liquid while also enhancing its removal. The following sections discuss liquid management as it relates to several relevant PEMFC topics.

## 6 Pressure and flow control

Liquid removal from reactant channels is facilitated primarily by aerodynamic drag forces. Higher gas flow rates reduce liquid buildup; however, they require greater pumping power. Ideally, designers would seek to operate a PEMFC at the lowest stoichiometry that maintains stable desired performance. For the cathode, the air compressor is adjusted to supply necessary flow rates and can be varied based on sensor feedback. For example, since liquid buildup leads to higher pressure drop, pressure transducer signals may be used to guide compressor speeds. On the anode, where hydrogen may be supplied from a pressurized tank, fuel distribution and utilization are a large concern, higher flow rates may be achieved using a circulating pump (*81*).

For stoichiometric-based gas control, higher flow channel velocities at elevated current densities have been shown to improve water management. In some cases, flooding may be more prevalent at lower current densities, despite lower water production, as gas pressure drop is not sufficient to push water out. Backpressure refers to the elevated flow-field pressure attained by restricting outflow gas using controllable valves. In some PEMFCs, higher back pressures are used to improve electrochemical performance by increasing reactant concentration and or by controlling gas routing in the flow field (*82*, *83*). Higher pressures mean greater gas density which increases the drag force on droplets. Some early work has shown that generating acoustic sound waves around 80 Hz in the reactant gases can enhance droplet detachment by inducing droplet vibration (*84*, *85*).

An overview of general PEMFC control schemes is available in Ref. (*86*). Recently the use of machine learning (ML) techniques has been explored for control, as well as to guide complex

design decisions in PEMFC. ML uses various algorithms, such as artificial neural networks (ANN) and decision trees (DT), which may be trained using large data sets to develop an analytical model with minimal human intervention. These models can be updated automatically as new information becomes available. Early work has used ML for the state of health estimation, flow-field design, two-phase flow analysis among others (*87–89*). Two-phase flow prediction, such as anticipating the onset of flooding, would be beneficial to PEMFC operation as instability and degradation events could be avoided. Recent studies have demonstrated the ability to map images of ex-situ PEMFC liquid water distributions with two-phase pressure drop (*90–92*). Eventually, complex dynamics between liquid, pressure drop, and overvoltage may be used to train ML systems for in-situ monitoring and control. Long short-term memory (LSTM) is a recurrent neural network (RNN) architecture used in the field of deep learning (*93*). Unlike standard feedforward neural networks, LSTM has feedback connections that allow it to process not only single data points but also entire sequences such as time-series data. LSTMs have recently been used to examine the use of time series two-phase pressure data to predict channel water build-up (*94*). Overall, ML implementation is in its early stages and may prove useful in developing future control and design schemes.

## 7 Thermal regulation and humidification

Heat is generated as a byproduct of PEMFC operation. Typically, steady-state PEMFC operation occurs between temperatures of 50°C and 80°C. Stacks usually require active cooling systems such as coolant channels between cells for thermal regulation. Reactant gas vapor pressure, as well as evaporation rates, are very sensitive to temperature. PEMFC systems commonly set the reactant gas humidity using dew point temperature control. Humid gases benefit membrane hydration; however, under humid conditions liquid may be prone to condense in diffusion media and channels. Dry gases have higher water uptake; however, membrane dehydration is a greater risk, especially in inlet regions and at higher flow rates. In a typical external humidification loop, water is evaporated into inlet gases from water condensed out of downstream gases.

Some systems, such as the Toyota Mirai, rely on internal circulation (self-humidification) to humidify gases which greatly reduces system complexity and cost. This is accomplished by running the anode gas stream counter to the cathode gas stream, which humidifies upstream airflow

(*81*). Researchers have recently demonstrated evaporative cooling using specially modified GDLs, where water flows through dedicated anode flow field channels, parallel to the gas channels, and is distributed over the cell area thanks to a modified GDL (*95*).

## 8 Startup/shutdown

Startup (or cold start when temperatures are subfreezing) refers to the transient process by which a dormant PEMFC is brought to its nominal operating conditions and power output. Usually, the goal is to achieve startup with minimal time and energy while avoiding cell degradation. During this period, cell or stack temperatures are below targets and must be ramped up to a steady state. Water production is related to the current which, during startup, may be ramped up continuously or in steps (*96*). Lower temperature gases have reduced capacity for water uptake and so water management during startup may be enhanced by supplying higher flow rates. Studies have shown improved startup performance at higher stoichiometry (*97*). The startup routine also depends on the way the cell was shut down. Various purge protocols exist to prepare a PEMFC for dormancy. The amount of water allowed to remain in the MEA and flow channels may depend on the duty cycle and environmental conditions. For normal operation, minimal purging may be required to clear channels while the membrane is left humid for efficient restart. The purge duration and intensity for a PEMFC being prepared for subfreezing conditions may be greater to prevent residual water. Water expands as it freezes which can lead to delamination and cracking of membrane and diffusion media (*98*). Degradation may be reduced via purging or by freeze prevention methods such as coolant loop antifreeze injection and thermal insulating.

Cold start is a challenge as ice, water, and vapor may exist simultaneously in the MEA. Understanding the dynamics of this multiphase process is necessary as many PEMFC applications encounter extreme cold temperature environments. Freezing temperatures can also affect other PEMFC subsystems containing nozzles and valves where ice formation leads to blockages. Cold start can be separated into two categories, assisted and unassisted. Assisted cold start refers to the use of resistance heating (powered by batteries) or heating of coolant loop fluids to warm the cell above freezing (*99*). While effective, these methods rely on other subsystems and can be energy-intensive. Unassisted cold start refers to the use of reaction waste heat to warm key cell components; therefore, the reaction takes place initially at cold temperatures. Cold startup

protocols may rely on hybrid strategies using both assisted and unassisted methods. During unassisted cold start water produced in the cCL condenses and begins to immediately fill the pore void space (*100*). If gas temperature and flow rate do not reach conditions where water uptake keeps up with production, the cCL floods and power output ceases. Water is also removed via back diffusion through the membrane and studies have shown cold start performance is tied to initial membrane hydration (*101*). While a drier membrane can improve cold start performance, the drying process can degrade the membrane; therefore, some level of residual water, even during freezing, may be beneficial. Cold start capability is also linked to MEA and flow-field design (*97*). Extensive numerical simulation of cold-start under varying conditions has shown that while low current densities during startup allow for higher pore space utilization, higher current densities produce waste heat at a higher rate per water production which may be beneficial to a cold start in certain scenarios (*102*, *102*, *103*). Due to land/wall heat conduction, ice was observed to appear first under land areas. Cold start cycling of an improperly purged MEA can lead to significant performance decline as well as hydrogen starvation causing irreversible electrode degradation (*104*). Overall, purging bulk water from channels and GDL while leaving some residual in the membrane and then using higher stoichiometries while initiating a current ramp-up are the basis for the successful unassisted startup.

## 9 Surface Ccoatings

Another strategy to influence liquid distribution is to alter the wetting properties of the channel walls and GDL through various hydrophobic and hydrophilic surface treatments. Droplet motion, characterized by contact angle hysteresis, is restrained by the pinned wetted perimeter of a droplet to a GDL and or channel surface (*19*). The pinning of a contact line results in a change in the shape of the liquid surface to accommodate pressure, gravitational, and shear forces without any bulk motion of the droplet. The difference between advancing and receding contact angles at the onset of motion is referred to as the maximum contact angle hysteresis (*18*). These dynamics allow a droplet to distort on the surface of the GDL without moving. Hydrophobic coatings have been shown to lower the maximum hysteresis and cause water to “bead-up” into smaller slugs which may be beneficial to purging processes and high current density operation. The influence of superhydrophobic coatings with static contact angled of >150° on PEMFC two-phase pressure

drop and liquid buildup is also being investigated (*105*). Some drawbacks are that hydrophobic and superhydrophobic channel walls may cause water to build up within GDL under land areas and cause droplets to have larger cross-sections normal to flow; therefore, these coatings should be applied strategically (*106*). Hydrophilic and superhydrophilic channel surfaces can improve liquid uptake from the GDL and under certain conditions result in film flow (*107*). This may benefit gas diffusion by keeping the GDL surface clear of water droplets which improves performance stability. The impact of long-term degradation on these coatings is not completely understood as thermal/mechanical stresses may reduce their effectiveness over time (*108*).

## 10 Ultra-thin electrodes

Ultra-thin low platinum group metal (PGM) loading electrode architectures are sought after to achieve high power density operation at a reduced cost. A major hurdle to their adoption is sensitivity to liquid water as their thinness provides less void space to accommodate simultaneous water uptake and gas diffusion (*109*). Two types, traditional Pt/C CL and nanostructured-thin-film (NSTF) CL, have received significant attention in recent years. Due to structural differences between the two, several strategies have been reported to mitigate flooding effects within them. For Pt/C designs, a thinner cathode MPL with higher air stoichiometry operation may enhance water removal (*8*). In NSTF CL, flooding was minimized by moving water out via the anode during low-temperature operation. This requires a thinner membrane or higher membrane permeability, removal of the anode MPL, and reduced anode pressure (i.e., $P_a < P_c$). Steinbach et al. performed systematic testing, including in-situ neutron imaging, of NSTF layers highlighting that, surprisingly, the anode side GDL had a large impact on performance (*48*). Further work improving GDL morphology for liquid-specific transport would benefit these scenarios where water back diffusion is utilized to relieve cCL flooding. Another potential challenge to ultra-thin architectures is increased gas crossover, especially oxygen moving from the cathode to the anode, and is the focus of some recent efforts.

## 11 Patterned and structured porous media

Structured porous media refers to media having a prescribed rather than random structure. Recently, a theoretical analysis of structured GDLs of various lattice configurations concluded that

significant performance improvements may be possible (*47*). Several groups have achieved enhancements by modifying traditionally manufactured MPLs and GDLs (*51*, *58*, *110*). A common goal among many efforts is to provide separate pathways for gas diffusion and liquid transport. For example, small perforations added to the MPL and GDL have been observed to improve liquid drainage leading to higher performance (*50*, *52*). Thumbarathy *et al.* (*110*, *111*) have recently demonstrated a spray coating technique where they used a mask with the desired pattern (stripes or polka dots) and a spray system to pattern GDL surfaces. They have designed GDLs with alternate stripes of two hydrophobic surfaces of different contact angles and with polka dots of a hydrophobic polymer of a higher contact angle than the base GDL. Their goal was to bias water pathways and provide favorable pathways to reactant gases to mitigate reactant starvation at high current densities. Figure 8.8(a) highlights the alternate stripes of two hydrophobic surfaces by spraying hydrophobic polymer using a patterned mask (such as fluorinated ethylene propylene (FEP) or a mixture of polydimethylsiloxane (PDMS) and fumed silica) on a conventional GDL surface (*110*). As the areas with higher contact angles will be difficult to penetrate by water, it will provide favorable pathways for reactant gases. The results shown by Thumbarathy *et al.* indicate that one can achieve over a 20% increase in limiting current with modified GDLs as compared with the unmodified GDLs (*110*). Groups have also demonstrated the inclusion of water pathways using radiation grafted hydrophilic patterning of traditional GDL materials (*112*). These approaches, while promising, are limited by the underlying GDL structure.

Advanced manufacturing techniques, such as microscale resolution 3D printing, may offer promising future solutions to these difficult problems. Two common printing methods are direct ink writing (DIW) and stereolithography (SL). DIW printing utilizes a position-controlled nozzle to extrude carbon ink filaments used to construct 3D structures. Inks for these systems must be thixotropic, that is, they flow under applied shear stress while returning to a self-supporting solid when the stress is removed (*113*). In SL printing, a UV-light source is used to form 3D objects by curing a resin in a bath layer by layer. Projected light, in the shape of the object's cross-section at a specific position, is focused on each corresponding layer by adjusting the height of the resin which is contained on a movable platform. Once all the features are cured, the remaining liquid resin is drained from the bath leaving only the desired structure and or support material. The process allows for intricate geometries and feature sizes <1 μm.

Lawrence Livermore National Laboratory (LLNL) has recently demonstrated the use of DIW 3D printed carbon aerogels (CA) in electrochemical systems such as electrolyzers and is currently probing PEMFC applications (*114*). CA are highly porous (> 95%) solid materials known for their very low density, high surface area, high electrical conductivity, thermal and chemical robustness, ultrafine open pore structure, and good mechanical properties (*113*). Figure 8.8 (b) shows a simple-cubic DIW printed CA structure; many other structures including body-centered cubic (BCC) lattices, face-centered cubic (FCC) lattices as well as gradient lattices and monoliths are being investigated (*113*). Pore gradient lattices could allow for liquid pathways utilizing differences in Laplace pressure to transport water away from flood-sensitive regions (*115*). In these electrodes since the filaments are highly porous aerogels created using a supercritical drying or freeze-drying process; reactant gas can diffuse through them, unlike the solid fibers of conventional GDL.

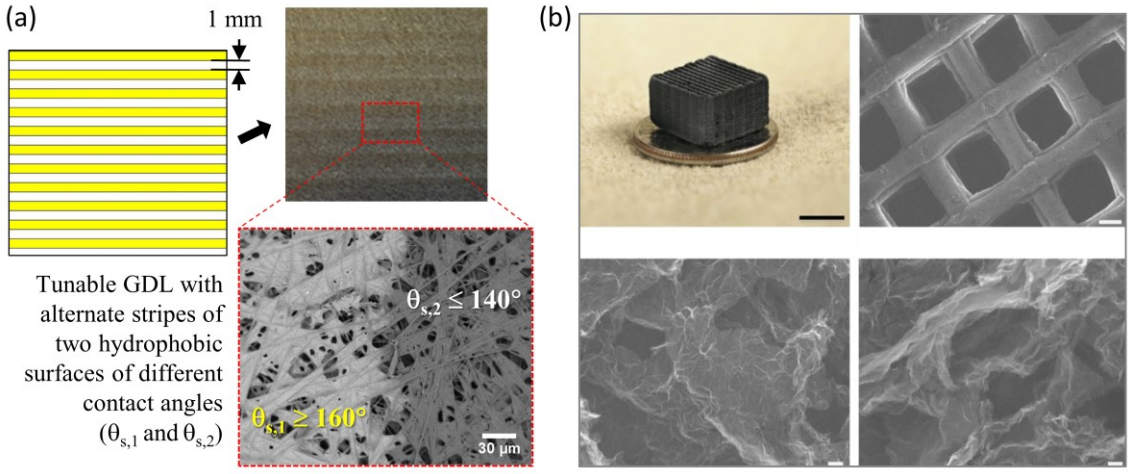


**FIGURE 8.8** (a) Additive manufacturing of alternate stripes of two hydrophobic surfaces of different contact angles (*110*) and (b) DIW printed carbon aerogel electrode - simple cubic structured lattice (*113*). *Credit: Part (a) is adapted from Thumbarathy et al., Journal of Electrochemical Energy Conversion and Storage,* ***17****(1), 011010, (2020), with permission from ASME, and Part (b) is from Chandrasekaran et al., Journal of Materials Research,* ***32****(22), 4166-4185, (2017).*

## 12 Summary

PEMFCs have the potential to play a significant role in helping industries such as heavy-duty trucking, shipping, rail, mobile power generation, and aerospace sectors reach low carbon emissions targets. To promote PEMFC adoption in these competitive markets, research and development must continue to seek solutions that reduce costs while increasing system lifetimes. Toward these pursuits, the management of liquid water should be considered a primary

engineering concern. This chapter highlights liquid transport mechanisms, two-phase flow behavior, operation strategies, and novel materials and manufacturing methods, which will offer new opportunities and challenges in this area. Knowledge of basic two-phase flow physics in porous media and channels offers engineers a practical starting point for understanding current architectures and for designing next-generation PEMFC systems.

## References


1. A. Z. Weber, J. Newman, *J. Electrochem. Soc.* **153**, A2205 (2006).
2. A. Z. Weber *et al.*, *Journal of The Electrochemical Society*. **161**, F1254–F1299 (2014).
3. G. Lin, W. He, T. Van Nguyen, *J. Electrochem. Soc.* **151**, A1999 (2004).
4. P. K. Das, X. Li, Z.-S. Liu, *International Journal of Hydrogen Energy*. **35**, 2403–2416 (2010).
5. G. S. Hwang, M. Kaviany, J. H. Nam, M. H. Kim, S. Y. Son, *J. Electrochem. Soc.* **156**, B1192 (2009).
6. E. F. Medici, J. S. Allen, *Journal of Power Sources*. **191**, 417–427 (2009).
7. P. K. Das, A. Grippin, A. Kwong, A. Z. Weber, *J. Electrochem. Soc.* **159**, B489–B496 (2012).
8. P. K. Das, A. Z. Weber, in *ASME 2013 11th International Conference on Fuel Cell Science, Engineering and Technology* (American Society of Mechanical Engineers, Minneapolis, Minnesota, USA, 2013; https://asmedigitalcollection.asme.org/FUELCELL/proceedings/FUELCELL2013/55522/Minneapolis,%20Minnesota,%20USA/228339), p. V001T01A002.
9. J. Benziger, J. Nehlsen, D. Blackwell, T. Brennan, J. Itescu, *Journal of Membrane Science*. **261**, 98–106 (2005).
10. Z. Lu, M. M. Daino, C. Rath, S. G. Kandlikar, *International Journal of Hydrogen Energy*. **35**, 4222–4233 (2010).
11. M. Mortazavi, K. Tajiri, *International Journal of Hydrogen Energy*. **39**, 9409–9419 (2014).
12. A. D. Santamaria, P. K. Das, J. C. MacDonald, A. Z. Weber, *J. Electrochem. Soc.* **161**, F1184–F1193 (2014).
13. F. Y. Zhang, X. G. Yang, C. Y. Wang, *J. Electrochem. Soc.* **153**, A225 (2006).

14. K. A. Triplett, S. M. Ghiaasiaan, S. I. Abdel-Khalik, A. LeMouel, B. N. McCord, *International Journal of Multiphase Flow*, 16 (1999).

15. K. A. Triplett, S. M. Ghiaasiaan, S. I. Abdel-Khalik, D. L. Sadowski, *International Journal of Multiphase Flow*, 18 (1999).

16. C. H. Schillberg, S. G. Kandlikar, in *ASME 5th International Conference on Nanochannels, Microchannels, and Minichannels* (ASMEDC, Puebla, Mexico, 2007; https://asmedigitalcollection.asme.org/ICNMM/proceedings/ICNMM2007/4272X/299/318387), pp. 299–310.

17. S. C. Cho, Y. Wang, K. S. Chen, *Journal of Power Sources*. **206**, 119–128 (2012).

18. E. C. Kumbur, K. V. Sharp, M. M. Mench, *Journal of Power Sources*. **161**, 333–345 (2006).

19. A. Theodorakakos *et al.*, *Journal of Colloid and Interface Science*. **300**, 673–687 (2006).

20. P. K. Das, A. D. Santamaria, A. Z. Weber, *Procedia Engineering*. **105**, 751–756 (2015).

21. A. D. Santamaria, J. Haydu, D. Senft, J. Riofrio, in *IMECE2015* (Volume 6B: Energy, 2015; https://doi.org/10.1115/IMECE2015-50651).

22. A. D. Santamaria, M. Mortazavi, *J. Electrochem. Soc.* **167**, 104507 (2020).

23. J. T. Sellman, A. D. Santamaria, *International Journal of Hydrogen Energy*. **42**, 12551–12558 (2017).

24. D. Spernjak, A. K. Prasad, S. G. Advani, *Journal of Power Sources*. **170**, 334–344 (2007).

25. I. V. Zenyuk, D. Y. Parkinson, G. Hwang, A. Z. Weber, *Electrochemistry Communications*. **53**, 24–28 (2015).

26. N. J. Cooper, A. D. Santamaria, M. K. Becton, J. W. Park, *International Journal of Hydrogen Energy*. **42**, 16269–16278 (2017).

27. A. D. Santamaria, M. K. Becton, N. J. Cooper, A. Z. Weber, J. W. Park, *Journal of Power Sources*. **293**, 162–169 (2015).

28. X.-G. Yang, N. Burke, C.-Y. Wang, K. Tajiri, K. Shinohara, *J. Electrochem. Soc.* **152**, A759 (2005).

29. Y. Shao *et al.*, *Energy Conversion and Management*. **185**, 169–182 (2019).

30. I. S. Hussaini, C.-Y. Wang, *Journal of Power Sources*. **187**, 444–451 (2009).

31. S. A. Niknam, M. Mortazavi, A. D. Santamaria, *Results in Engineering*. **5**, 100071 (2020).

32. M. Mortazavi, K. Tajiri, *Renewable and Sustainable Energy Reviews*. **45**, 296–317 (2015).

33. R. Banerjee, S. G. Kandlikar, *Journal of Power Sources*. **247**, 9–19 (2014).

34. R. Banerjee, S. G. Kandlikar, *Journal of Power Sources*. **268**, 194–203 (2014).

35. M. Grimm, E. J. See, S. G. Kandlikar, *International Journal of Hydrogen Energy*. **37**, 12489–12503 (2012).

36. M. Mortazavi *et al.*, *Journal of Electrochemical Energy Conversion and Storage*. **18** (2021), doi:10.1115/1.4049572.

37. R.W. Lockhart, R.C. Martinelli, *Chem. Eng.* **45**, 39–48 (1949).

38. D. Chisholm, *Int. J. Heat Mass Transf.* **10**, 1767–1778 (1967).

39. S. Saisorn, S. Wongwises, *Experimental Thermal and Fluid Science*. **34**, 454–462 (2010).

40. M. Mortazavi, M. Heidari, S. A. Niknam, *null*. **41**, 1784–1799 (2020).

41. J. Benner, M. Mortazavi, A. D. Santamaria, in *IMECE2018* (Volume 6A: Energy, 2018; https://doi.org/10.1115/IMECE2018-86579).

42. I. V. Zenyuk, E. Medici, J. Allen, A. Z. Weber, *International Journal of Hydrogen Energy*. **40**, 16831–16845 (2015).

43. N. J. Cooper, A. D. Santamaria, M. K. Becton, J. W. Park, *Energy Conversion and Management*. **136**, 307–317 (2017).

44. A. D. Santamaria, N. J. Cooper, M. K. Becton, J. W. Park, *International Journal of Hydrogen Energy*. **38**, 16253–16263 (2013).

45. A. D. Santamaria, J. Bachman, J. W. Park, *International Journal of Hydrogen Energy*. **38**, 5807–5812 (2013).

46. Larminie, James, Andrew Dicks, and Maurice S. McDonald, *Fuel cell systems explained* (Wiley, 2003), vol. 2.

47. D. Niblett, V. Niasar, S. Holmes, *J. Electrochem. Soc.* **167**, 013520 (2020).

48. A. J. Steinbach *et al.*, *Joule*. **2**, 1297–1312 (2018).

49. J. Becker, C. Wieser, S. Fell, K. Steiner, *International Journal of Heat and Mass Transfer*. **54**, 1360–1368 (2011).

50. A. Mohseninia *et al.*, *ChemSusChem*. **13**, 2931–2934 (2020).

51. Y. Nagai *et al.*, *Journal of Power Sources*. **435**, 226809 (2019).

52. D. Gerteisen, T. Heilmann, C. Ziegler, *Journal of Power Sources*. **177**, 348–354 (2008).

53. A. Lamibrac *et al.*, *J. Electrochem. Soc.* **163**, F202–F209 (2016).

54. J. T. Gostick, M. A. Ioannidis, M. W. Fowler, M. D. Pritzker, *Journal of Power Sources*. **173**, 277–290 (2007).

55. K.-J. Lee, J. H. Nam, C.-J. Kim, *Journal of Power Sources*. **195**, 130–141 (2010).

56. P. K. Sinha, C.-Y. Wang, *Electrochimica Acta*. **52**, 7936–7945 (2007).

57. P. Chippar, K. O, K. Kang, H. Ju, *International Journal of Hydrogen Energy*. **37**, 6326–6338 (2012).

58. M. Balakrishnan *et al.*, *ACS Appl. Energy Mater.* **3**, 2695–2707 (2020).

59. N. J. Cooper, T. L. Smith, A. D. Santamaria, J. Wan Park, *Journal of Electrochemical Energy Conversion and Storage*. **15**, 041006 (2018).

60. N. J. Cooper, T. Smith, A. D. Santamaria, J. W. Park, *International Journal of Hydrogen Energy*. **41**, 1213–1223 (2016).

61. J. Scholta *et al.*, *Journal of Power Sources*. **155**, 66–71 (2006).

62. T. L. Smith, A. D. Santamaria, J. W. Park, K. Yamazaki, *Procedia CIRP*. **14**, 275–280 (2014).

63. S.-W. Cha, R. O'Hayre, S. J. Lee, Y. Saito, F. B. Prinz, *J. Electrochem. Soc.* **151**, A1856 (2004).

64. S. W. Cha, R. O'Hayre, Y. Saito, F. B. Prinz, *Journal of Power Sources*. **134**, 57–71 (2004).

65. J. Park, X. Li, *Journal of Power Sources*. **163**, 853–863 (2007).

66. N. Akhtar *et al.*, *International Journal of Hydrogen Energy*. **34**, 3104–3111 (2009).

67. J. Bachman *et al.*, *International Journal of Hydrogen Energy*. **37**, 17172–17179 (2012).

68. Y. Sando, *ECS Trans.* **25**, 211–224 (2009).

69. A. Iranzo, C. H. Arredondo, A. M. Kannan, F. Rosa, *Energy*. **190**, 116435 (2020).

70. N. Kizilova, M. Sauermoser, S. Kjelstrup, B. G. Pollet, *Entropy*. **22**, 176 (2020).

71. C.-J. Tseng *et al.*, *Energy Conversion and Management*. **62**, 14–21 (2012).

72. A. Santamaria, J. Zhang, in *FEDSM2017* (Volume 1B, Symposia: Fluid Measurement and Instrumentation; Fluid Dynamics of Wind Energy; Renewable and Sustainable Energy Conversion; Energy and Process Engineering; Microfluidics and Nanofluidics; Development and Applications in Computational Fluid Dynamics; DNS/LES and Hybrid RANS/LES Methods, 2017; https://doi.org/10.1115/FEDSM2017-69358).

73. M. Kim, C. Kim, Y. Sohn, *Fuel Cells*. **18**, 123–128 (2018).

74. J. E. Park *et al.*, *International Journal of Hydrogen Energy*. **44**, 22074–22084 (2019).

75. Z. Bao, Y. Wang, K. Jiao, *Journal of Power Sources*. **480**, 229150 (2020).

76. T. Yoshida, K. Kojima, *Interface magazine*. **24**, 45–49 (2015).

77. S. G. Kandlikar, W. J. Grande, *Heat Transfer Engineering*. **24**, 3–17 (2003).

78. P. Concus, R. Finn, *Proceedings of the National Academy of Sciences of the United States of America*. **63**, 292–299 (1969).

79. C. D. Rath, S. G. Kandlikar, *Colloids and Surfaces A: Physicochemical and Engineering Aspects*. **384**, 653–660 (2011).

80. S. H. Han, N. H. Choi, Y. D. Choi, *Renewable Energy*. **44**, 88–98 (2012).

81. H. Lohse-Busch, K. Stutenberg, M. Duoba, S. Iliev, "Technology Assessment Of A Fuel Cell Vehicle: 2017 Toyota Mirai" (United States, 2018), , doi:10.2172/1463251.

82. J. Bachman, A. Santamaria, H.-Y. Tang, J. W. Park, *Journal of Power Sources*. **198**, 143–148 (2012).

83. S. Tong, J. C. Bachman, A. Santamaria, J. W. Park, *Journal of Power Sources*. **242**, 195–201 (2013).

84. M. Mortazavi, A. D. Santamaria, J. Z. Benner, V. Chauhan, *J. Electrochem. Soc.* **166**, F3143–F3153 (2019).

85. A. M. Schafer, J. S. Allen, *ECS Trans.* **41**, 1887–1896 (2011).

86. W. R. W. Daud *et al.*, *Renewable Energy*. **113**, 620–638 (2017).

87. V. Chauhan, M. Mortazavi, J. Z. Benner, A. D. Santamaria, *Energy Reports*. **6**, 2713–2719 (2020).

88. S. Laribi, K. Mammar, Y. Sahli, K. Koussa, *Sustainable Energy Technologies and Assessments*. **34**, 35–42 (2019).

89. H. Pourrahmani, M. Moghimi, M. Siavashi, M. Shirbani, *Applied Thermal Engineering*. **150**, 433–444 (2019).

90. A. D. Santamaria, *Journal of The Electrochemical Society*, 12 (2021).

91. A. D. Santamaria *et al.*, *ECS Transactions*. **98**, 279 (2020).

92. A. D. Santamaria, M. Mortazavi, V. Chauhan, J. Benner, in *ECS Meeting Abstracts* (IOP Publishing, 2019), p. 1538.

93. S. Hochreiter, J. Schmidhuber, *Neural Computation*. **9**, 1735–1780 (1997).

94. Jingru Benner, Mehdi Mortazavi, Vedang Chauhan, Oliver K. Philbrick, Anthony D. Santamaria, in *ASTFE Proceedings* (Las Vegas, Nevada, USA, 2022).

95. M. Cochet *et al.*, *Fuel Cells*. **18**, 619–626 (2018).

96. K. Tajiri, Y. Tabuchi, C.-Y. Wang, *Journal of The Electrochemical Society*. **154**, B147 (2006).

97. A. D. Santamaria, J. Bachman, J. W. Park, *Electrochimica Acta*. **107**, 327–338 (2013).

98. X. G. Yang, Y. Tabuchi, F. Kagami, C.-Y. Wang, *Journal of The Electrochemical Society*. **155**, B752 (2008).

99. Q. Guo, Y. Luo, K. Jiao, *International Journal of Hydrogen Energy*. **38**, 1004–1015 (2013).

100. L. Mao, C.-Y. Wang, *J. Electrochem. Soc.* **154**, B139 (2007).

101. J. Ko, H. Ju, *Applied Energy*. **94**, 364–374 (2012).

102. K. Jiao, X. Li, *International Journal of Hydrogen Energy*. **35**, 5077–5094 (2010).

103. K. Jiao, X. Li, *Electrochimica Acta*. **54**, 6876–6891 (2009).

104. H. Chen, X. Zhao, T. Zhang, P. Pei, *Energy Conversion and Management*. **182**, 282–298 (2019).

105. A. D. Santamaria *et al.*, *ECS Transactions*. **104**, 221 (2021).

106. A. Turhan, S. Kim, M. Hatzell, M. M. Mench, *Electrochimica Acta*. **55**, 2734–2745 (2010).

107. H.-Y. Tang, A. Santamaria, J. W. Park, C. Lee, W. Hwang, *Journal of Power Sources*. **196**, 9373–9381 (2011).

108. F. A. De Bruijn, V. A. T. Dam, G. J. M. Janssen, *Fuel cells*. **8**, 3–22 (2008).

109. I. V. Zenyuk, P. K. Das, A. Z. Weber, *Journal of the Electrochemical Society*. **163**, F691 (2016).

110. D. Thumbarathy, G. Gupta, M. Mamlouk, P. K. Das, *Journal of Electrochemical Energy Conversion and Storage*. **17**, 011010 (2020).

111. D. Thumbarathy, P. K. Das, in *Electrochemical Conference on Energy and the Environment: Bioelectrochemistry and Energy Storage* (Electrochemical Society, Glasgow, 2019; https://doi.org/10.1149/MA2019-04/3/169).

112. A. Forner-Cuenca *et al.*, *Advanced materials*. **27**, 6317–6322 (2015).

113. S. Chandrasekaran, P. G. Campbell, T. F. Baumann, M. A. Worsley, *Journal of Materials Research*. **32**, 4166–4185 (2017).

114. V. A. Beck *et al.*, *Proceedings of the National Academy of Sciences*. **118** (2021).

115. Anthony D. Santamaria, Swetha Chandrasekaran, Oliver K. Philbrick, Marcus Worsley, in *ECS Transactions* (The Electrochemical Society, Vancouver, BC, Canada, 2022).